



## Synthesis of high-entropy Ti-Zr-Nb-Hf-Ta carbides and carbonitrides in high-speed arc discharge plasma jet

Dmitry S. Nikitin <sup>a</sup>, Ivan I. Shanenkov <sup>a,b</sup>, Artur R. Nassyrbayev <sup>a</sup>, Alexander A. Sivkov <sup>a,c</sup>, Viktor S. Baidyshev <sup>d</sup>, Yulia A. Kvashnina <sup>e</sup>, Nikita A. Matsokin <sup>d</sup>, Alexander Ya. Pak <sup>a</sup>, Alexander G. Kvashnin <sup>d,\*</sup>

<sup>a</sup> National Research Tomsk Polytechnic University, 30 Lenin Avenue, Tomsk 634050, Russia

<sup>b</sup> University of Tyumen, 6 Volodarskogo st., Tyumen 625003, Russia

<sup>c</sup> College of Communication Engineering, Jilin University, Changchun 130023, PR China

<sup>d</sup> Skolkovo Institute of Science and Technology, Skolkovo Innovation Center, Bolshoy Boulevard 30, bld. 1, Moscow 121205, Russia

<sup>e</sup> Pirogov Russian National Research Medical University, 1 Ostrovityanova St., Moscow, Russia

### ARTICLE INFO

#### Keywords:

High-entropy carbides  
High-entropy nitrides  
Nanomaterials  
Plasma dynamic synthesis  
Computational discovery

### ABSTRACT

The interest in high-entropy materials has increased rapidly in recent decades due to their applications in various fields such as environmental barrier coatings, superhard and wear resistant coatings, nuclear energy, batteries, catalysts, thermoelectrics, supercapacitors, biocompatible structures, and microelectronics. In the present work, comprehensive theoretical and experimental studies are carried out to discover a new way to prepare high-entropy ceramic nanopowders of carbides and carbonitrides of IV-V transition metals. The possibility of  $(\text{TiZrNbHfTa})\text{C}_x\text{N}_y$  formation is investigated using both ab initio and machine learning approaches. The chosen single-stage plasma dynamic technique allowed us to synthesize high-entropy carbide  $\text{TiZrNbHfTaC}_5$  and the corresponding carbonitrides (N up to 8 wt%) in the form of single-crystalline nanoparticles. By varying the experimental system conditions, we demonstrate not only the production of pure powders, but also the ability to apply different precursors, including pure metals and their oxides. The presented technique provides a simple and universal way to produce high-entropy nanomaterials and opens the door to the synthesis of many functional ceramic powders composed of other carbonitrides with selective nitrogen content.

### 1. Introduction

With the development of aerospace technology, there is a high demand for thermal protection system (TPS) materials that are resistant to high-temperature oxidation, thermal shock and ablation [1,2]. For this reason, the interest in high-entropy materials (HEM) is growing rapidly from day to day. HEM have unique and intriguing properties that allow these materials to be used in structural and functional areas with harsh operating conditions [3–5]. The new field of materials science related to high-entropy compounds was started from the extensive studies on high-entropy alloys (HEA) [6,7]. Since then the list of HEMs has continued to grow. Studies of HEAs have been replaced by studies of high-entropy ceramics, which are also defined as a solid solution of five

or more cation or anion sublattices with high configurational entropy [8]. Such ceramics include many classes of materials, and there is now work on the synthesis of high-entropy oxides [9–14], borides [15–20], carbides [3,21–25], silicides [26–29], sulfides [30–32], nitrides [33–36] etc. Among the above groups of materials, metal carbides, carbonitrides and nitrides are the most interesting for applications as oxygen-free ultra-high-temperature ceramics (UHTCs) due to their high hardness, oxidation resistance and refractoriness compared to the corresponding mono-compounds [37,38]. Thus, the idea of increasing the elemental composition of compounds using the high-entropy concept to achieve outstanding properties has potential [34,39].

The most promising in terms of the possibility of forming a single-phase compound are the IV and V group metal carbides, which are

\* Corresponding author.

E-mail address: [A.Kvashnin@skoltech.ru](mailto:A.Kvashnin@skoltech.ru) (A.G. Kvashnin).

characterized by mutual complete solubility between each of them (except VC) [40,41]. In this system, TiZrNbHfTaC<sub>5</sub> stands out as an ideal high-entropy carbide (HEC) with a NaCl-type cubic crystal lattice and the most potential candidate material for structural elements in high-temperature applications due to its high mechanical properties (hardness of 15–27 GPa, Young's modulus of 350–550 GPa and fracture toughness of 3–6 MPa·m<sup>1/2</sup>) and temperature stability (above 1500 °C) [42,43]. However, the synthesis of TiZrNbHfTaC<sub>5</sub>, as well as HEC in general, is extremely labor-intensive, because it is carried out at high temperatures of about 2200–2300 °C for a long time during the process itself and the preparation (homogenization) of the feedstock [43,44]. The inability to achieve the necessary synthesis conditions is known to be the main reason for the unsatisfactory results in the synthesis of high-entropy carbides and their derivatives [25].

Even more challenging is the introduction of nitrogen into the HEC structure and the formation of the corresponding high-entropy carbonitrides (HECN). Attempts have been made to synthesize HECN using various experimental techniques. The synthesis of (Ti<sub>0.25</sub>V<sub>0.25</sub>Nb<sub>0.25</sub>Ta<sub>0.25</sub>)(C<sub>1-x</sub>N<sub>x</sub>) with different nitrogen compositions (x = 0, 0.1, 0.2, 0.3) was performed by ball milling a mixture of carbide and nitride powders followed by spark plasma sintering [45]. Jing et al. [46] used low temperature carbothermal reduction nitriding to synthesize powders of (Ti<sub>0.2</sub>V<sub>0.2</sub>Nb<sub>0.2</sub>Ta<sub>0.2</sub>Mo<sub>0.2</sub>)(C<sub>0.9</sub>N<sub>0.1</sub>). The same method, but at a higher temperature of 1400 °C, was used by Ma et al. [47] to synthesize (HfZrTaNbTi)(C,N) in a flowing N<sub>2</sub> atmosphere. Hot-press sintering at 1500 °C was used by Wen et al. [48] to synthesize (Hf<sub>0.2</sub>Zr<sub>0.2</sub>Ta<sub>0.2</sub>Nb<sub>0.2</sub>Ti<sub>0.2</sub>)(N<sub>0.5</sub>C<sub>0.5</sub>) high-entropy carbonitride.

The analysis of the presented results allows one to identify several peculiarities of the existing methods. 1) Preference is given to methods that include a stage of high-temperature exposure stage, which leads to recrystallization and the impossibility of obtaining nanomaterials. 2) The processes can take from several hours to a day and are energy

$$F_{\text{vib}}(V, T) = k_B T \int_0^{\omega_{\text{max}}} g(\omega(V)) \ln \left[ 1 - \exp \left( -\frac{\hbar\omega(V)}{k_B T} \right) \right] d\omega + \frac{1}{2} \int g(\omega(V)) \hbar\omega d\omega \quad (3)$$

intensive with low efficiency and high carbon footprint. 3) High requirements for reaction precursors, probability of contamination of the final products and difficulty in achieving the required composition and stoichiometry of the final compound. The necessary conditions for the synthesis of HEC and HECN are possible when using thermal plasma methods [24,49]. However, even in this case, there is a significant particle growth due to prolonged plasma exposure, which prevents the formation of nanostructures. In this respect, pulsed single-stage electric arc methods with the possibility of controlling the final phase composition and low precursor requirements can be considered as an alternative for the synthesis of HEC and HECN.

Here we present the results of the synthesis of high-entropy carbide and carbonitride (TiZrNbHfTa)C<sub>x</sub>N<sub>y</sub> in the form of nanopowders using, for the first time, high-speed jet of pulsed arc discharge plasma. The ability of mixing of individual carbides and nitrides in the (TiZrNbHfTa)C<sub>x</sub>N<sub>y</sub> structures is studied by density functional theory, the experimental studies are performed to demonstrate the possibility of varying the HECN composition depending on the initial conditions of the synthesis system (material of electrodes, type of precursors, gas medium).

## 2. Methods

### 2.1. Computational details

To determine the most stable concentration of nitrogen in the considered high-entropy carbonitrides (HECNs) we calculate the

mixture of individual metal carbides (TiC, ZrC, NbC, HfC, TaC) and nitrides (TiN, ZrN, NbN, HfN, TaN) using the enthalpy of mixing with addition of configurational entropy as  $\Delta G_{\text{mix}}(T) = G_{\text{mix}}(T) - TS_{\text{mix}}$  [50, 51].

Here  $G_{\text{mix}}$  is the free energy of mixing, which can be calculated as follows:

$$G_{\text{mix}}(T) = \frac{G_{\text{tot}}(T) - \sum_i M_i G_i^{\text{MeC}}(T) - \sum_j N_j G_j^{\text{MeN}}(T)}{\sum_i M_i + \sum_j N_j} \quad (1)$$

where  $G_{\text{tot}}$  is the Helmholtz free energy of the considered multi-component carbide at a given temperature,  $G_i^{\text{MeC}}$ ,  $G_j^{\text{MeN}}$  are the Helmholtz free energies of individual metal carbides and nitrides, respectively,  $M_i$ ,  $N_j$  are the number of individual metal carbides and nitrides. The total number of individual carbides and nitrides ( $i+j$ ) remains constant for all considered structures.

Our calculations are based on density functional theory (DFT) [52, 53] within the generalized gradient approximation (the Perdew–Burke–Ernzerhof functional) [54] and the projector augmented wave method [55,56] as implemented in the VASP [57–59] code. The plane wave energy cutoff of 400 eV, the Methfessel–Paxton smearing [60] of electronic occupations, and  $\Gamma$ -centered k-point meshes with a resolution of  $2\pi \times 0.025\text{\AA}^{-1}$  for the Brillouin zone sampling are used, ensuring the convergence of the energy differences and stress tensors.

The Helmholtz free energy for a given structure is calculated as follows

$$G_{\text{tot}}(T) = E_0(V) + F_{\text{vib}}(V, T) \quad (2)$$

where  $E_0$  is the total energy from the DFT calculations,  $F_{\text{vib}}$  is the Helmholtz vibrational free energy calculated in the harmonic approximation from the following relationship [61]

Here  $g(\omega(V))$  is the phonon density of states at a given volume, calculated using the finite displacement method as implemented in PHONOPY [62,63] with forces calculated using VASP [57–59].

The mixing entropy  $S_{\text{mix}}$  in the homogeneous limit can be determined by using the Boltzmann entropy formula:

$$S_{\text{mix}} = k_B \left( \sum_{i=1}^C x_i \ln x_i + \sum_{j=1}^N y_j \ln y_j \right) \quad (4)$$

where  $k_B$  is the Boltzmann constant,  $x_i$  and  $y_i$  are the mixing concentrations of individual carbides and nitrides in the considered HECNs,  $C$  and  $N$  are the numbers of metal carbides and nitrides respectively in the considered HECNs.

The Helmholtz free energy of formation for the considered structures is calculated using the following formula:

$$G_{\text{form}}(T) = \frac{G_{\text{tot}}(T) - \sum_i n_i G_i^{\text{Me}}(T) - n_N G^{\text{N}}(T) - n_C G^{\text{C}}(T)}{\sum_i n_i + n_N + n_C} \quad (5)$$

where  $G_{\text{tot}}$  is the Helmholtz free energy of the considered multi-component carbide at a given temperature,  $G_i^{\text{Me}}$  is the Helmholtz free energy of individual metals,  $n_i$ ,  $n_N$ , and  $n_C$  are the number of individual metals in the structure, and the number of nitrogen and carbon atoms, respectively.

The lattice size difference parameter is another property that can be used to estimate the formation ability of HECN and can be calculated as follows:

$$\delta = \sqrt{\sum_{i=1}^{n_C} x_i \left[ \left( 1 - \frac{a_i^C}{\sum_{i=1}^{n_C} x_i a_i^C + \sum_{i=1}^{n_N} (1-x_i) a_i^N} \right)^2 + \left( 1 - \frac{c_i^C}{\sum_{i=1}^{n_C} x_i c_i^C + \sum_{i=1}^{n_N} (1-x_i) c_i^N} \right)^2 \right] + \sum_{i=1}^{n_N} (1-x_i) \left[ \left( 1 - \frac{a_i^N}{\sum_{i=1}^{n_C} x_i a_i^C + \sum_{i=1}^{n_N} (1-x_i) a_i^N} \right)^2 + \left( 1 - \frac{c_i^N}{\sum_{i=1}^{n_C} x_i c_i^C + \sum_{i=1}^{n_N} (1-x_i) c_i^N} \right)^2 \right]} \quad (6)$$

where  $a_i^C$ ,  $a_i^N$ ,  $c_i^C$ ,  $c_i^N$  are the lattice constants of the  $i^{\text{th}}$  individual transition metal carbides and nitrides,  $x_i$  is the molar fraction of carbides in the HECN,  $n_N$ , and  $n_C$  are the number of individual nitrides and carbides in the HECH.

To perform such DFT calculations, we generated  $2 \times 2 \times 2$  supercells with the rocksalt crystal structure containing 32 metal atoms and 32 non-metal atoms. The generation of a random disordered distribution of metal atoms and then nitrogen atoms over the supercell is done by using the VASPKIT package [64]. In this way 7 HECH (the increment of the nitrogen content is 0.125), 1 HEC and 1 HEN structures are generated.

All generated structures along with individual carbides (TiC, ZrC, NbC, HfC, TaC) and nitrides (TiN, ZrN, NbN, HfN, TaN) are relaxed using the VASP code [57–59].

Geometry relaxation of the considered structures was performed in the LAMMPS package [65]. The interaction between atoms in the HECH structures is described by a neural network potential, trained using the DP-GEN method as implemented in the DeePMD-kit [66]. The sizes of the embedding and fitting nets are set to (25, 50, 100) and (120, 120, 120), respectively. The cut-off radius is set to 6 Å. Each model is trained with 5000 gradient descent steps with an exponentially decaying learning rate from  $10^{-4}$  to  $10^{-8}$ .

The neural network potential is trained on the ab initio molecular dynamics (AIMD) trajectories. The AIMD simulation for each nitrogen concentration is performed for 2000 steps with a timestep of 0.5 fs using the same DFT parameters described above. Constant temperature is controlled by Nosé-Hoover thermostat [67,68]. Angular and radial descriptors are included in the model, with a cutoff-radius of 6.0 Å.

## 2.2. Experimental details

The plasma dynamic synthesis method is used to synthesize high-entropy carbides and carbonitrides. The detailed description of the system is given in previous works [69,70]. In general, this method consists of using high-speed arc discharge plasma jet as a medium for high-energy plasma-chemical synthesis reactions. The arc discharge and subsequent plasma flux are generated using a coaxial magnetoplasma accelerator (Figure S1 in the Supporting Information). This device combines both a central electrode and a coaxial barrel electrode, which are rigidly fixed and insulated from each other in such a way that an arc discharge geometry is created in the gap between them, the so-called plasma formation zone. In this region the precursor mixture  $m_{\text{mix}}$  is placed in dispersed form.

For the chosen HECH material, both titanium and graphite electrode systems have been investigated to determine which one is better for the synthesis of high-entropy compounds  $(\text{TiZrNbHfTa})_{\text{x}}\text{Ny}$ . The titanium electrode system allows the production of the main metallic precursor (Ti) by electrical erosion of the barrel electrode, which has been demonstrated for materials such as  $\text{TiO}_2$ ,  $\text{TiB}_2$  and some other titanium-containing compounds [69,71]. The graphite electrode system is characterized by the possibility of achieving higher temperatures and pressures in the generated plasma (up to 25000 K and 8 MPa, respectively, at a current of up to 100 kA) [72], which allows the synthesis of refractory compounds through the liquid phase state [70,73,74].

The considered system is extremely universal in terms of synthesis conditions and initial energy parameters, which are varied by the

charging conditions of the capacitive energy storage used to power the plasma accelerator. For the chosen electrode systems, the initial energy parameters were  $W_c = 27$  kJ,  $U_c = 3.0$  kV,  $C_c = 6.0$  µF, taking into account the mechanical stability of the electrode system with respect to the electrodynamic loads created during the flow of the discharge current with a magnitude  $> 10^5$  A. When the potential difference exceeds 2 kV in the plasma formation zone located between the central and barrel electrodes, the interelectrode gap is broken, accompanied by the conversion of precursors to the plasma state. The plasma jet is accelerated by the magnetic fields of the barrel electrode and the inductor and flows into the chamber reactor filled with inert gas (argon) at room temperature and atmospheric pressure (see Figure S1 in the Supporting Information).

Discharge current and voltage during synthesis are recorded using Tektronix TDS2012 oscilloscopes through the Rogowski coil and ohmic voltage divider respectively. The recorded data are used to calculate energy characteristics such as maximum arc voltage ( $U_{\text{max}}$ ), amplitude of discharge current ( $I_{\text{max}}$ ), amplitude of discharge power ( $P_{\text{max}}$ ), value of energy released ( $W$ ), pulse duration ( $t_{\text{imp}}$ ), average value of discharge power ( $P_{\text{av}}$ ).

The synthesized dispersed material with a mass of  $\sim 0.35$  g per unit cycle (with an initial precursors mixture mass of 0.5 g) with a duration of less than 1 ms is collected from the reaction chamber. Pre-preparation of the precursors included grinding and mixing the components to the required mass ratio. Two types of components are used, such as powders of pure metals Ti, Zr, Nb, Hf, Ta (Rare Metals corp., Russia, purity 99.9 %, average size  $\leq 10$  µm) or metal oxides  $\text{TiO}_2$ ,  $\text{ZrO}_2$ ,  $\text{Nb}_2\text{O}_5$ ,  $\text{HfO}_2$ ,  $\text{Ta}_2\text{O}_5$  (Rare Metals corp., Russia, purity 99.9 %, average size  $\leq 10$  µm). Sibunite (Federal Research Centre Boreskov Institute of Catalysis, Russia, purity 99.0 %, surface area  $\sim 340$  m<sup>2</sup>/g) is used as the carbon source. The proportions of components used in the synthesis of a metal composition with equimolar and five times the atomic content of carbon in the final  $\text{TiZrNbHfTaC}_5$  material are displayed in Table S1 of the Supporting Information. Eq The equiatomic selection of metals is consistent with the traditional concept of high-entropy materials, defined as "those composed of five or more principal elements in equimolar proportions." [6]. The results of the experiments carried out to synthesize powders of high-entropy compounds are summarized in Table S2 in the Supporting Information and allow us to conclude that they can be compared due to the proximity of the process energetics.

X-ray diffraction patterns (Figures S2-S5 in the Supporting Information) of the initial components together with mixtures of metals,  $\text{Me}+\text{C}$ ,  $\text{MeO}$ , and  $\text{MeO}+\text{C}$  show the reactionless formation of the  $\text{Ti-Zr-Nb-Hf-Ta-(C)}$  mixture at the machining stage. Figures S6-S8 in the Supporting Information show scanning electron microscopy (SEM) images of individual components and their mixtures. Both the initial powder metals and their oxides differ in their particle size distribution, but processing allows us to grind large particles and thus achieve sufficient averaging of precursor dispersion and significantly reduce the variation in particle size. In addition, plasma dynamic synthesis involves plasma treatment of precursors under extreme energy conditions, allowing the ignition of components that differ significantly in size and structure.

The final synthesized materials without further processing are studied by analytical methods. The phase composition of the synthesized

and initial raw materials are analyzed by X-ray diffraction methods using a Shimadzu XRD-7000 X-ray diffractometer 7000 ( $\text{CuK}\alpha 1$ -irradiation,  $\lambda_1 = 1.5406 \text{ \AA}$ ,  $2\theta = 10\text{--}90 \text{ deg}$ ). Diffraction reflections are identified using the Crystallographica Search-Match program and the PDF4+ structure database. The average value of the lattice constant  $a$  of high-entropy compounds with cubic structure is determined from the position of the X-ray maxima  $2\theta_{\text{hkl}}$  with Miller indices (111), (200), (220), (311), (222), (400) and the corresponding interplanar distances  $d_{\text{hkl}}$ .

To study the microstructure of the dispersed synthesis products and initial raw materials, scanning electron microscopy analysis is performed using Hitachi TM3000 and Thermo Fisher Scientific Apreo S LoVac microscopes, together with Tescan Mira 3LMU and Quanta 200 3D systems with X-ray energy dispersive microanalysis (EDS). Transmission electron microscopy analysis is performed using a Phillips CM 12 microscope.

The direct identification of nitrogen atoms in the chemical bonds of the synthesized high-entropy compounds is performed by X-ray photo-electron spectroscopy using a SPECS GmbH system (SPECS Surface Nano Analysis GmbH, Germany) with a PHOIBOS 150 WAL hemispherical analyzer and a non-monochromatic X-ray source ( $\text{Al-K}\alpha$  radiation 1486.6 eV, 200 W). The obtained spectra are processed using Avantage Thermo Fisher and CasaXPS software (version 2.3.15, CASA Software Ltd., Teignmouth, UK).

### 3. Results and discussions

To establish the fundamental feasibility of producing high-entropy compounds, several experiments are carried out using different electrode systems (the main parameters are listed in [Tables S1, S2](#) in the Supporting Information). Considering the versatility of the plasma dynamic system in terms of the possibility of using different precursors (pure metals and their oxides), experimental studies are carried out to determine the most effective one by studying different mixtures consisting of pure metals ( $\text{Me}$ ,  $\text{Me+C}$ ) and metal oxides ( $\text{MeO}$ ,  $\text{MeO+C}$ ). The proportions of the components in the prepared mixtures of precursors are summarized in [Table S3](#) in the Supporting Information.

In addition, in the graphite electrode system, three potentially feasible types of materials are attempted to be synthesized in the  $(\text{TiZrNbHfTa})\text{C}_x\text{N}_y$  system, namely high-entropy carbides (HEC), when  $y = 0$ , high-entropy carbonitrides (HECN), when  $0 < x < 1$  and  $0 < y < 1$ , and high-entropy nitrides (HEN), when  $x = 0$ . To obtain HEC, carbon-containing precursor mixtures ( $\text{Me+C}$ ,  $\text{MeO+C}$ ) are used, while the reaction chamber is filled with argon as the gaseous medium. For HECN, precursor mixtures containing carbon ( $\text{Me+C}$ ,  $\text{MeO+C}$ ) are used, followed by nitrogen filling of the reaction chamber ([Tables S1, S2](#) in the Supporting Information). For HEN, precursor mixtures without carbon ( $\text{Me}$ ,  $\text{MeO}$ ) are placed in the plasma formation zone, and the reactor chamber was subsequently filled with nitrogen.

Prior to this, a series of experiments are carried out (see Supporting Information, [Figures S9-S12](#)) to justify the choice of carbon precursor and the method of precursor preparation. Scanning electron microscopy images of products obtained from different precursors are shown in [Figures S13-S16](#) in the Supporting Information.

Their microstructure analysis indicates the formation of highly dispersed materials in the form of dense agglomerates with sizes up to several microns. Each particle within the agglomerate has an average size of up to 100 nm with no significant size differences (see [Figure S17](#) in the Supporting Information). For each series, no significant changes in material composition are observed when the mixture of precursors based on pure metals is replaced by a mixture containing metal oxides. This suggests that, due to the extreme conditions of the process, the plasma dynamic synthesis method is not critical in the choice of metal precursor in terms of the final product microstructure. Nanoscale particles of the synthesis products are formed from nanoscale liquid-phase droplets of the molten precursor mixture under high-speed sputtering conditions due to the supersonic plasma flow velocity ( $> 1 \text{ km/s}$ ). These nanoscale liquid droplets are then crystallized at high cooling rates (not less than  $10^7 \text{ K/s}$ ) [75]. Due to the high surface energy, such particles can form dense agglomerates. The products also contain larger objects in the powder, but these do not exceed 300 nm.

Energy-dispersive X-ray spectroscopy (EDS) is used to analyze the elemental composition. [Table 1](#) shows the results of the semi-quantitative EDS analysis of areas around  $10 \times 10 \mu\text{m}$  in the form of mass fractions. There are practically no oxygen peaks confirming the complete elimination of oxygen from the product when metal oxides are used as precursors (see [Figures S18-S23](#) in the Supporting Information). This is due to the likely participation of oxygen in the combustion reaction of the liquid-phase carbon from the plasma jet as  $\text{C} + \text{O}_2 \rightarrow \text{CO}_2$ . This fact confirms the fundamental advantage of the plasma dynamic synthesis method, which is the possibility of using cheaper and more abundant precursors in the form of metal oxides.

It is worth noting that the carbon content of the samples varies by approximately 20 % based on the analysis data. However, these results are not accurate due to the imaging performed on a graphite tape. The increase in carbon content in the samples obtained from the graphite electrode system can be attributed to the electrical erosion of the graphite barrel electrode during the synthesis process. Additionally, the initiation of the arc discharge is due to the application of a thin conducting layer of graphite aerosol on the surface of the precursor mixture placed in the plasma formation zone. Based on the stoichiometry of the  $\text{TiZrNbHfTaC}_5$ , the estimated carbon content should be approximately 9 %.

The content of metals in the products obtained in the graphite electrode system, when converting the results into atomic fractions of elements (the mass ratio should be 7:14:14:14:27:27:10 for  $\text{Ti:Zr:Nb:Hf:Ta}$ ), satisfies the equiatomic ratio as well as the initial ratio in the precursor mixture. However, the results obtained for the titanium electrode system (first row in [Table 1](#)) are noteworthy because the titanium content significantly exceeds the equiatomic fraction. This is also due to the electrical erosion of the titanium barrel electrode and the entry of excess eroded titanium into the plasma-chemical reaction zone.

The key finding from the elemental analysis is the consistent variation in the nitrogen content of the synthesis products produced in the graphite electrode system. When the products are generated in an inert medium without nitrogen, the nitrogen concentration of 1–2 wt%. When the nitrogen atmosphere is applied, the content increases to 2–4 %.

**Table 1**  
Results of X-ray energy dispersive microanalysis of synthesis products.

Electrode system	Compound to be synthesized	Mixture	$\omega(\text{C})$ , %	$\omega(\text{N})$ , %	$\omega(\text{Ti})$ , %	$\omega(\text{Zr})$ , %	$\omega(\text{Nb})$ , %	$\omega(\text{Hf})$ , %	$\omega(\text{Ta})$ , %	Total, %
Ti	HEN	Me	44.24	34.31	20.28	0.24	0.15	0.44	0.34	100
		MeO	6.11	26.9	65.25	0.36	0.52	0.41	0.44	100
C	HEC	Me+C	19.97	1.03	6.35	12.36	9.79	24.72	25.78	100
		MeO+C	20.39	1.86	12.21	13.69	11.83	22.31	17.72	100
	HECN	Me+C	23.55	3.58	7.24	13.01	9.98	21.87	20.78	100
		MeO+C	19.68	2.06	12.4	14.48	13.13	21.21	17.05	100
	HEN	Me	11.96	4.91	6.57	12.76	11.32	26.85	25.63	100
		MeO	23.41	7.95	4.56	8.00	12.84	17.12	26.11	100

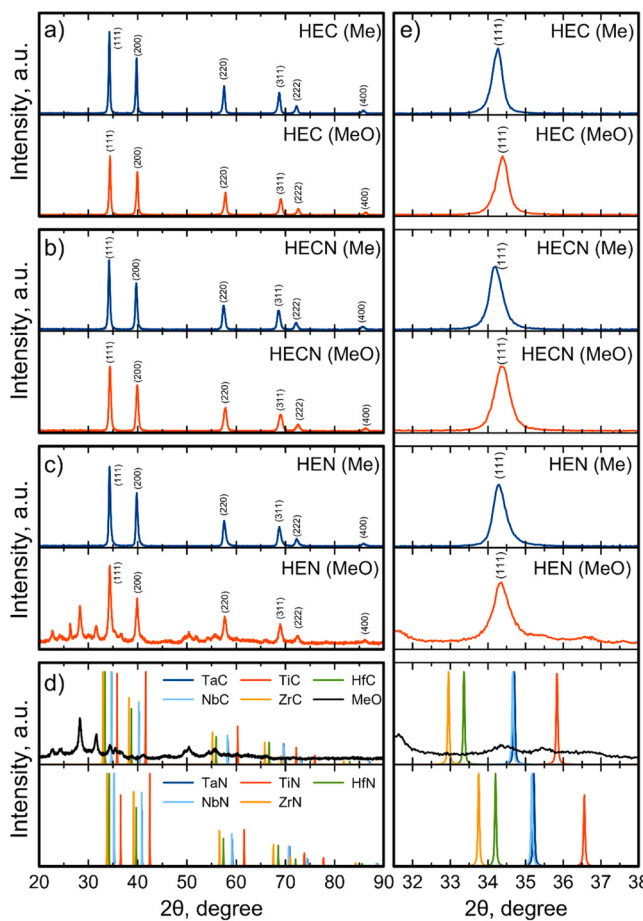


**Fig. 1.** X-ray diffraction patterns of a) HEC, b) HECN, and c) HEN products obtained in the graphite electrode system from the raw powder of Me and MeO in comparison with reference d) XRD patterns of individual carbides and nitrides. e) Enlarged region  $2\theta = 32\text{--}38$  deg near (111) reflection.

An even higher nitrogen content of up to 5–8 % can be obtained by using a carbon-free mixture (Me and MeO instead of Me+C and MeO+C respectively). This nitrogen content is close to its mass content in the hypothetical compound  $\text{TiZrNbHfTa}_{\text{N}_5}$  (10.59 %). However, the lower nitrogen content may indicate the incomplete formation of nitride or, in conjunction with the presence of carbon, the formation of stoichiometric carbonitride ( $\text{TiZrNbHfTaC}_{\text{x}}\text{N}_{\text{y}}$  where  $\text{x} \approx \text{y}$  is approximately 2.5).

The titanium electrode system shows a significantly higher nitrogen content of roughly 30 %, which, taking into account the error of the method, is close to the value of 22.58 % associated with the nitrogen fraction in the TiN compound [76]. The distribution of the detected chemical elements for the “potentially HEN” sample obtained using the nitrogen atmosphere and a mixture without carbon (Me) as precursor is shown in Figure S24 in the Supporting Information. It can be easily observed that all chemical elements from the high-entropy compound composition, including Ti, Zr, Nb, Hf, Ta, as well as C and N, are uniformly distributed in the product, indicating the chemical homogeneity of the product based on the high-entropy compound  $\text{TiZrNbHfTaC}_{\text{x}}\text{N}_{\text{y}}$ . Information on the XRD patterns and their description can be found in the Supporting Information and Figure S25. Measured lattice constants of the single-crystal cubic phase obtained from the synthesis process are presented in Table S4 in the Supporting Information. The data clearly indicate the formation of titanium nitride TiN in the titanium electrode system.

More informative results can be achieved within the graphite electrode system as there is no significant excess of certain metals. Fig. 1 shows the X-ray diffraction patterns of products synthesized in the

graphite electrode system. In general there is little change in the character of the XRD patterns despite the HEC-HECN-HEN transition (Fig. 1a,b,c). Furthermore, the use of metal and metal oxide based precursor mixtures yields the same result. All products are single-phase and all have a cubic crystalline phase with the FCC rocksalt structure with an  $Fm\bar{3}m$  (no. 225) space group. Based on the position of the intensity maxima, this cubic phase does not correspond to any of the individual carbides or nitrides of the considered metals. Furthermore, the absence of peaks of unreacted precursors in the XRD patterns suggests that a single-phase high-entropy compound containing atoms from all five metals has formed.

For the synthesized crystalline phases the lattice constants are calculated and presented in Table S4 in the Supporting information. It was observed that the lattice parameters of all the obtained crystalline phases are close to  $\text{TiZrNbHfTaC}_5$ . It can also be clearly concluded that the pure high-entropy nitride is not formed in any case. At the same time, considering the unambiguous data of elemental analysis, we can assume the partial incorporation of nitrogen atoms into the structure of  $\text{TiZrNbHfTaC}_5$  with practical preservation of the unit cell parameters in the case of experiments using the nitrogen atmosphere and a mixture without carbon (Me or MeO).

Another important fact is the presence of significant intensity peaks of unreacted precursors in the X-ray patterns in the case of the MeO mixture without carbon (Fig. 1d). This indicates incomplete ignition of the precursors due to the low conductivity of the oxide mixture. When the arc discharge is initiated by graphitization, the precursors are then sublimated by discharge over the surface of the plasma formation zone rather than by volumetric discharge in the powder cavity. Therefore, the use of the MeO oxide mixture for the synthesis of high-entropy materials in the considered system requires the mandatory addition of an electrically conductive component (predominantly carbon).

According to the results of the X-ray analysis, it is currently not possible to obtain  $\text{TiZrNbHfTa}_{\text{N}_5}$  nitride in a graphite electrode system. A possible solution would be to use a carbon-free mixture of MeO as a precursor. In this case, the excess carbon from electrical erosion is destroyed by oxidation of carbon from the decomposed oxide, but it is not possible to achieve full initiation of the arc discharge and ignition of the precursors. In general, the complete elimination of carbon in the system to produce nitrides is not possible today. The first reason is that the use of a graphite electrode system is the most promising in terms of the extreme conditions created. This leads to the introduction of additional eroded graphite into the chemical reaction and thus into the final product. The second reason is the need to ensure sufficient conductivity of the precursor mixture, which should be provided by the addition of carbon.

To understand the possibility of formation of high-entropy compounds, we have performed *ab initio* simulations of several  $\text{TiZrNbHfTaC}_{1-x}\text{N}_x$  structures with the increment of nitrogen content  $x$  of 0.125. The crystal structures of the considered  $\text{TiZrNbHfTaC}_{1-x}\text{N}_x$  with  $x = 0, 0.5, 1$  (HEC, HECN, and HEN) with 64 atoms in the unit cell are shown in Fig. 2a. In the HECN structures, nitrogen and carbon atoms are randomly distributed in the crystal volume and occupy 4b Wyckoff positions, while metal atoms occupy 4a Wyckoff positions.

The simulated X-ray diffraction patterns for the considered high-entropy carbonitrides with different nitrogen concentrations are shown in Fig. 2b-d. It can be seen that the experimental XRD for HEC (both Me and MeO) is in good agreement with the simulated one (Fig. 2b). This further confirms that the applied method of synthesis can be used to produce high-entropy carbides without complicated sample and feedstock preparation.

Considering different concentrations of nitrogen in the structure we observed a slight shift of the main reflections of the simulated structures towards larger angles compared to HEC (Fig. 2c). However, it should be noted that experimentally obtained XRD reflections for (111) and (200) planes are more consistent with a high-entropy carbide than a nitride.

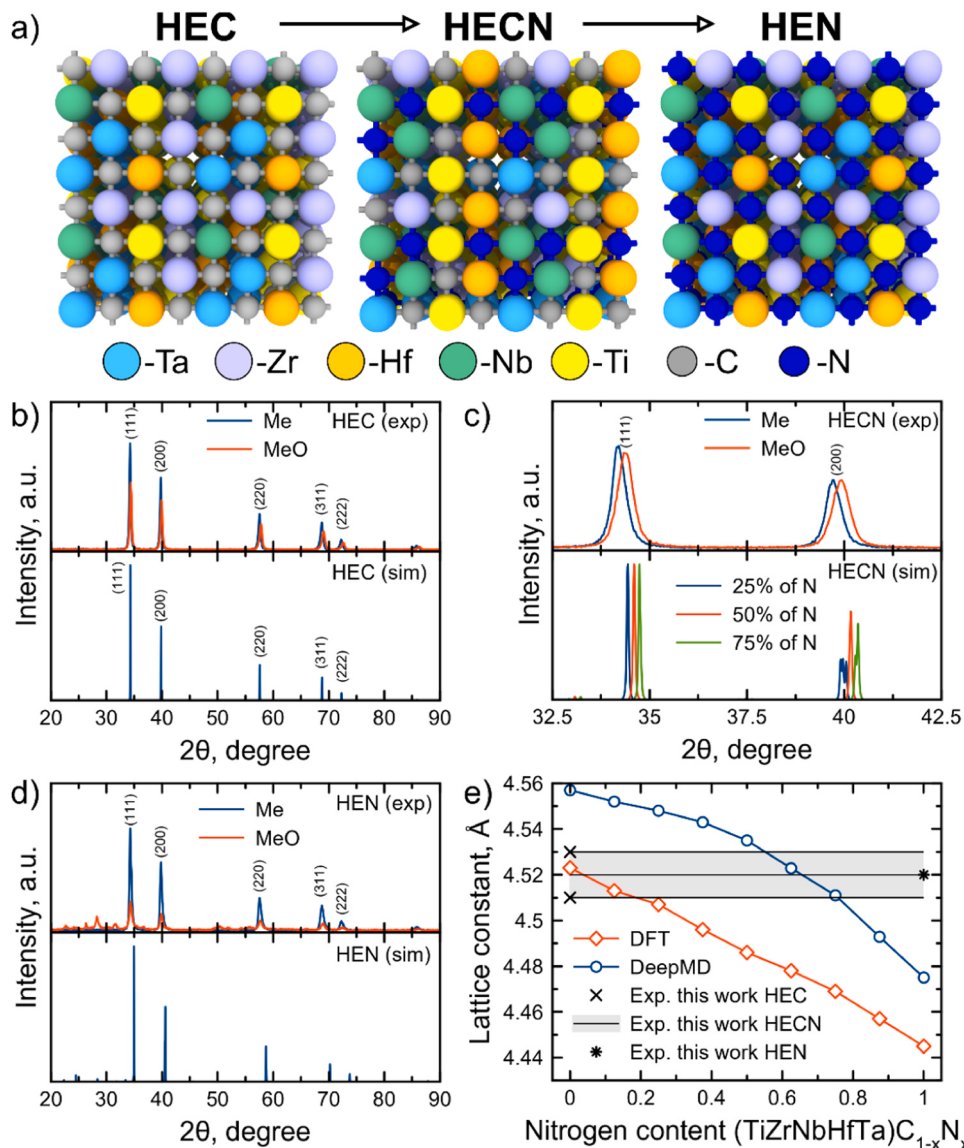


**Fig. 2.** a) Crystal structures of simulated unit cells of HEC, HEZN, and HEN. Carbon atoms are represented by grey spheres, nitrogen by blue, tantalum by light blue, zirconium by light pink, hafnium by orange, niobium by green, and titanium by yellow. Experimentally measured and simulated XRD patterns for b) HEC, c) HEZN (enlarged region from 32.5 to 42.5 degrees is shown), and d) HEN. Simulations of XRD for HEZN were performed for nitrogen contents 25, 50, and 75 %. e) Dependence of lattice parameters on nitrogen content calculated using DFT and DeepMD in comparison with experimental data (crosses and asterisks).

This may be a sign that we have not been able to incorporate the nitrogen in the desired concentration into the fcc lattice experimentally.

The complete substitution of carbon by nitrogen leads to an even larger shift of the simulated reflections towards the higher angles (Fig. 2d). However, there is not much difference between the experimentally measured XRD of HEC and HEZN (see Fig. 2b and Fig. 2d for the Me series), which could be explained by the formation of HEC instead of HEN, since the nitrogen concentration in the HEN sample is quite low (see Table 1). This is an important point, and it will be discussed later.

Calculated lattice parameters of simulated structures as a function of nitrogen content compared to experimentally measured ones are shown in Fig. 2e. The lattice constants are analyzed both for small unit cells from DFT calculations (64 atoms) and for large structures (4096 atoms) relaxed by the trained DeepMD potential. The calculated lattice constants compared to the experimental ones are presented in Tables S5 and S6 in the Supporting information. One can see that DeepMD yields lattice constants about 1 % higher than the DFT data (Fig. 2e). However, this overestimation leads to an inconsistency with the experimental

data. If we compare the DFT lattice parameters with the experimental ones for HEC, we see a good agreement:  $a_{\text{exp}} = 4.510\text{--}4.530 \text{ \AA}$ ,  $a_{\text{theory}} = 4.523 \text{ \AA}$ . This result is also in agreement with our previous work [24] where we synthesized HEC  $\text{TiZrNbHfTaC}_5$  using the vacuumless arc-charge plasma technique.

As the amount of nitrogen in the synthesized HEZN  $\text{TiZrNbHfTaC}_{1-x}\text{N}_x$  cannot be accurately determined we have plotted the measured lattice parameters for HEZN as horizontal lines in Fig. 2e. As mentioned above, the lattice parameters for HEZN  $\text{TiZrNbHfTaC}_{1-x}\text{N}_x$  matches with those measured for HEC. Comparison of the experimental lattice parameters for HEZN with our DFT simulations gives us an estimate of the nitrogen content ranging from 0 % to 20 %.

The results of our simulations show that despite the presence of a nitrogen atmosphere during synthesis, there is very little incorporation of nitrogen into the cubic lattice to form high-entropy nitride. However, the formation of metal-carbon and metal-nitrogen bonds in a single structure does occurs as can be seen from the Raman and XPS measurements below.

The formation of HEZN is studied by calculating the Helmholtz free

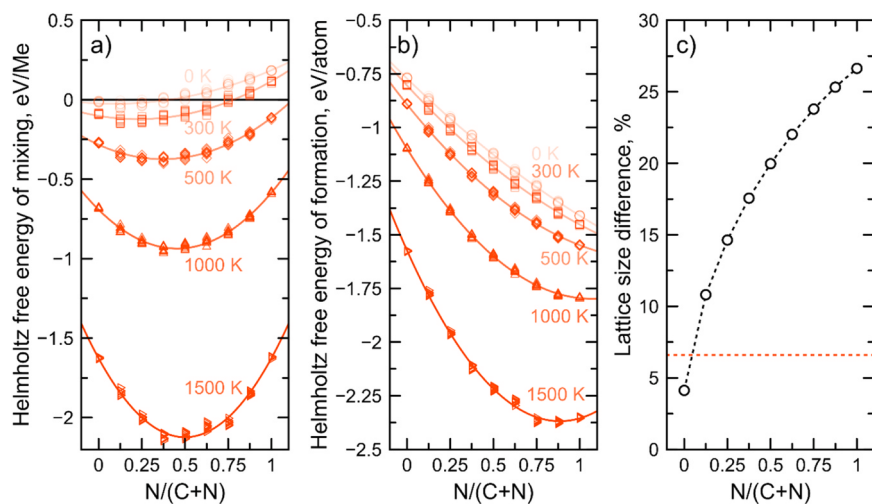


**Fig. 3.** Calculated Helmholtz free energy of a) mixing and b) formation of the considered HECN with different nitrogen contents. For each composition ten structures with uniformly distributed metal and non-metal atoms on the lattice were considered and calculated. c) Lattice size difference as a function of nitrogen concentration. The dashed horizontal line is the critical lattice size difference [77].

energy of mixing (see Eq. (1)) and the Helmholtz free energy of formation (see Eq. (5)) as a function of the nitrogen content, see Fig. 3a,b. For each nitrogen content in HECN ten different structures with uniformly distributed metal and non-metal atoms were considered. The difference between the total energies calculated for the considered configurations within a composition is less than 1 % (ten configurations for each composition). According to the mixing energy calculations, it is energetically unfavorable for five individual metal carbides and nitrides to mix in a single-phase solid solution at 0 K, see Fig. 3a. As the temperature increases the Helmholtz free energy of mixing becomes negative, and the minimum energy is reached at 37.5 % or 50 % of the nitrogen concentration.

The Helmholtz enthalpy of mixing cannot be used as a good descriptor of the probability of formation of HECN because there are not all individual nitrides have an fcc structure. Cubic polymorphic modifications of niobium and tantalum nitrides are less stable than hexagonal ones. Gibbs free energies of formation calculated using DFT-PBE and DFT-SCAN approximations to describe the electron exchange correlation (XC) for cubic and hexagonal polymorphic modifications of NbN and TaN are shown in the Supporting Information (Figure S26). Similar results have been reported in Ref. [78]. Furthermore, according to our calculations, cubic modifications of TaN and NbN are dynamically unstable with imaginary phonon modes, as can be seen from the calculated phonon density of states (Figure S27 in the Supporting Information). Both methods (DFT-PBE and SCAN) showed this difference in dynamic stability.

The calculated Helmholtz free energy of formation (Fig. 3b) shows that the formation of HEN is energetically more favorable than the formation of HEC and intermediate HECNs as the temperature is lower than 1000 K. Higher temperature (1500 K) leads to a minimum corresponding to 87.5 % of nitrogen in HECN. Thus, energetically, the formation of HECN and HEN should be the most favorable process if we consider the formation from the gas phase consisting of nitrogen, carbon and metals, which are at the same level. Similar conclusions have been reached previously for individual metal carbides and nitrides [79–83]. According to our formation energy calculations, compounds with nitrogen have lower formation energies and are therefore preferable. However, from an experimental point of view, if carbon is present in the system, the formation of carbides, including high-entropy carbides, is a more favorable process. If all carbon is removed from the system, leaving only nitrogen, the probability of nitride formation increases. This can be explained by considering the binding energies of the C-C bonds in graphite and the N-N bonds in the N<sub>2</sub> molecule. As nitrogen is in

the gas phase in the reaction chamber and carbon is present as a graphite electrode, the density of carbon is much greater than that of nitrogen. Therefore, during electrode erosion, metals can interact with a greater amount of carbon than nitrogen. In addition, the bond dissociation energy of the N<sub>2</sub> molecule is 9.79 eV [84], which is 1.5 times greater than that of carbon (6.29 eV [84]). As a result, it is much easier to extract carbon from the graphite electrode than to break the strong N-N bond to allow nitrogen to interact with metals.

It is also necessary to consider the kinetics and time of the carbide and nitride formation reactions. The combination of metals and carbon into carbide already occurs during the process of plasma jet acceleration. At the same time, N<sub>2</sub> as a nitrogen precursor is only expressed when the plasma jet flows into the reactor chamber, to a greater extent during the expansion of the structure. In this case, given the further deceleration of the plasma jet, the drop in temperature, the low concentration of the nitrogen precursor and the partially completed synthesis of carbide, the probability of complete nitride formation is low. However, the partial introduction of nitrogen into the carbide crystal structure and the formation of carbonitride is not excluded. One of the ways of optimizing the plasma dynamic synthesis to increase the probability of the formation of the high-entropy carbonitrides and nitrides is to reduce the erosion of the electrode system, which can be achieved both by

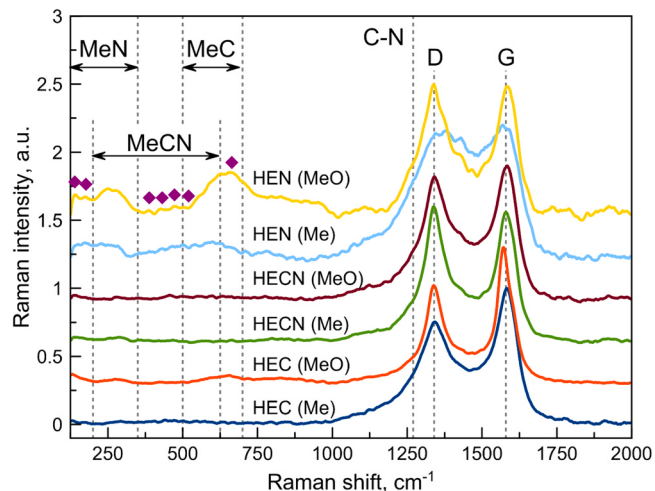


**Fig. 4.** Raman spectra of synthesized HEC, HECN and HEN products obtained from raw Me and MeO powders.

improving the design of the electrode system and by choosing a more suitable electrode material (in particular based on refractory metals such as Zr, Nb, Hf, Ta) [17].

Another property that allows us to estimate the ability of HECN to form is the lattice size difference ( $\delta$ ), which can be calculated using Eq. (6). As can be seen from Fig. 3c the lattice size difference increases with increasing nitrogen content. It has been pointed out by Yang et al. [77] that the critical  $\delta$  below which the formation of high-entropy material is possible is about 6.6 %, see the dashed horizontal line in Fig. 3c. This analysis shows that the formation of carbonitride is not possible due to large lattice mismatches between individual carbides and nitrides and the resulting mechanical stresses. According to this data, the critical nitrogen concentration in the HECN corresponding to the critical lattice size difference should be 2.5 %.

It can be concluded that the formation of HECN with high nitrogen content is a thermodynamically favorable process. However, the difference between the structures of individual carbides and nitrides may be unfavorable to the formation of high-entropy carbonitride. In other words, the reflections measured by Raman and XPS (see below) may be caused by small amounts of nitrogen incorporated into the HEC lattice.

However, difficulties in the formation of high-entropy nitrides do not imply the impossibility of partial incorporation of nitrogen into the crystal structure of the products, as confirmed by the results of energy-dispersive analysis. We have used Raman spectroscopy and X-ray photoelectron spectroscopy (XPS) analysis to fully confirm the ideas about the formation of Me-N chemical bonds in the final materials.

Fig. 4 shows the results of Raman measurements of HEC, HECN, and HEN products obtained from the mixture of pure metals (Me) and metal oxides (MeO). The obtained spectra show typical characteristics of metal-containing materials [85]. It should also be noted that carbides (including high-entropy ones) are usually quite weak in Raman spectra and therefore these results cannot be taken as unambiguous evidence for the presence/absence of carbides [22,86]. Rather, they serve to characterize the carbon in the product, as well as the bonds of oxide and nitrogen compounds [87,88]. Two broad intense reflections around  $1360 - 1570 \text{ cm}^{-1}$  can be observed in all samples, corresponding to D and G peaks of carbon. Presence of D and G peaks identifies the formation of C-C bonds within the graphitic structure [89]. The results obtained indicate the formation of a composite material containing TiZrNbHfTa-based compound as the major phase and ordered (D, amorphous) and disordered (G, graphite-like) carbon structures. The remaining carbon is contained in carbon-metal bonds, indicated by peaks in the  $500 - 700 \text{ cm}^{-1}$  range [90–92].

The possible formation of metal-nitrogen bonds can be indicated by peaks in the range  $200 - 350 \text{ cm}^{-1}$  [90–92], which appear in the spectra of materials obtained in a nitrogen atmosphere (mixtures of Me and MeO). It has been suggested in Ref. [93] that the existence of Me-C-N bonds is evidenced by the peaks located between the Me-N and Me-C bands of the Raman spectra, see Fig. 4. We have observed small kinks in the region around  $1270 \text{ cm}^{-1}$ , which are characteristic of C-N vibrational modes [94].

In addition, Raman data indicate the presence of amorphous materials in the HEN products. In the HEN (MeO) sample, such amorphous by-products are unreacted precursors in the form of metal oxides characterized by the presence of corresponding peaks [95–97]. In the HEN (Me) sample, such oxides are absent, so carbon with broader D and G peaks may act as such an amorphous component.

The state of chemical bonding and elemental composition of the obtained materials are investigated by XPS method. Fig. 5 shows the XPS spectra of the Ti2p, Zr3d, Nb3d, Hf4f, Ta4f, C1s, and N1s regions for the synthesized product with the highest nitrogen content in the composition (HECN, Me; spectra for all other samples are given in Figures S28–S32 in the Supporting Information). Intensity maxima are identified based on known reference data [98] and an available database of spectra recorded for Aldrich powders [99]. Overview of XPS spectra shows that Ti, Zr, Nb, Hf, Ta, C atoms can be detected in all products, nitrogen is

identified in products obtained in nitrogen atmosphere (HECN, HEN).

For the XPS data of metals shown in Fig. 5, the peaks  $\text{Ti}2\text{p}_{3/2}$  at 454.95 eV and  $\text{Ti}2\text{p}_{1/2}$  at 461.13 eV are correlated with Ti-N bonds;  $\text{Zr}3\text{d}_{5/2}$  at 179.67 eV and  $\text{Zr}3\text{d}_{3/2}$  at 182.20 eV are correlated with Zr-N or Zr-O bonds;  $\text{Nb}3\text{d}_{5/2}$  at 204.01 eV and  $\text{Nb}3\text{d}_{3/2}$  at 206.78 eV, are associated with Nb-N bonds;  $\text{Hf}4\text{f}_{7/2}$  at 14.57 eV and  $\text{Hf}4\text{f}_{5/2}$  at 16.26 eV indicate the presence of Hf-C or Hf-N bonds;  $\text{Ta}4\text{f}_{7/2}$  at 23.56 eV and  $\text{Ta}2\text{p}_{5/2}$  at 25.49 eV, are correlated with Ta-C or Ta-N bonds. In addition, for the N1s spectrum, bonds with metals (Ti and/or Nb and/or Zr) are identified for the peaks at 397.13 eV, see Fig. 5. This clearly identifies metal-nitrogen bonds in the HEN product. In addition to metal-nitrogen bonds, carbon-nitrogen bonds (C-N or C≡N for the peaks at 285.41 and 286.62 eV) may also be present. The simultaneous presence of metal bonds with nitrogen and carbon (Me-N and Me-C bonds, where Me = Ti, Zr, Nb, Hf, Ta) can be seen. This confirms the formation of the previously proposed structure with the Ti-Zr-Nb-Hf-Ta-C-N composition with the presence of both carbon and nitrogen in the nodes of the crystal lattice.

The analysis of the whole set of XPS spectra for all the series of obtained products revealed the intrinsic peculiarity, namely that the materials obtained in the argon medium are characterized by a more unambiguous interpretation of the position of the XPS peaks in the metal-carbon bond region. This is logical given the absence of free nitrogen in the reaction system. The XPS results also identify oxygen and the bonds of principal components with it. This indicates oxidation of the surface of the dispersed material (probably during storage and transport, since the samples are not pre-treated prior to analysis). This effect is typical of nitrides and carbides of transition metals due to their high reactivity with oxygen [100].

The quantitative XPS results, including the atomic concentrations of the analyzed elements are presented in Table S6 in the Supporting Information. One should note that in the absence of nitrogen in the system (HEC series), the minimum nitrogen content in the product is obtained (at the level of the statistical error of the method), while the nitrogen content reaches 8 % (for HECN and HEN series) when the synthesis is carried out in a nitrogen atmosphere. The nitrogen content typically corresponds to the metal content (1.5–4 %) and can indicate the formation of a structure that is close to equiatomic.

The microstructure of the synthesized materials is also examined by transmission electron microscopy (TEM), as shown in Fig. 6. The selected area electron diffraction (SAED) patterns obtained for HEC, HECN, and HEN represent a set of point reflections of crystalline phases, see Fig. 6a-c. The observed set of reflections forms separate characteristic Debye rings with an estimated value of the interplanar distance corresponding to the crystalline phase with the  $Fm\bar{3}m$  structure previously identified by XRD.

An overview micrograph of the synthesized products presented in Fig. 6d-f shows the formation of a series of crystalline nanoparticles. The average size of all the nanoparticles is much smaller than 100 nm (see Fig. 6d-f). At the same time, the product obtained in the argon environment (HEC) is characterized by the presence of a number of larger nanoparticles with a size around 150 nm (Fig. 6d). This is due to the different thermophysical properties of the gases in the chamber-reactor (nitrogen or argon). In particular, the thermal conductivity coefficient (0.0165 W/m•K for argon, 0.0259 W/m•K for nitrogen), which affects the heat dissipation from the synthesized liquid-phase material and the crystallization rate of the particles. A slight increase in particle size is observed with HEN compared to HECN, which may be due to a change in the properties of the reaction zone rather than the gases in the reactor. When the aperture diaphragm is shifted into the reflective region of the cubic phase, the reflective planes of characteristic polyhedral particles with sizes of several tens of nanometers appear (Fig. 6g-l).

In addition, the SAED shows an amorphous halo typical of carbon structures with an interplanar spacing corresponding to the set of (002) crystal planes of graphite, see Fig. 6a-c. The presence of such carbon

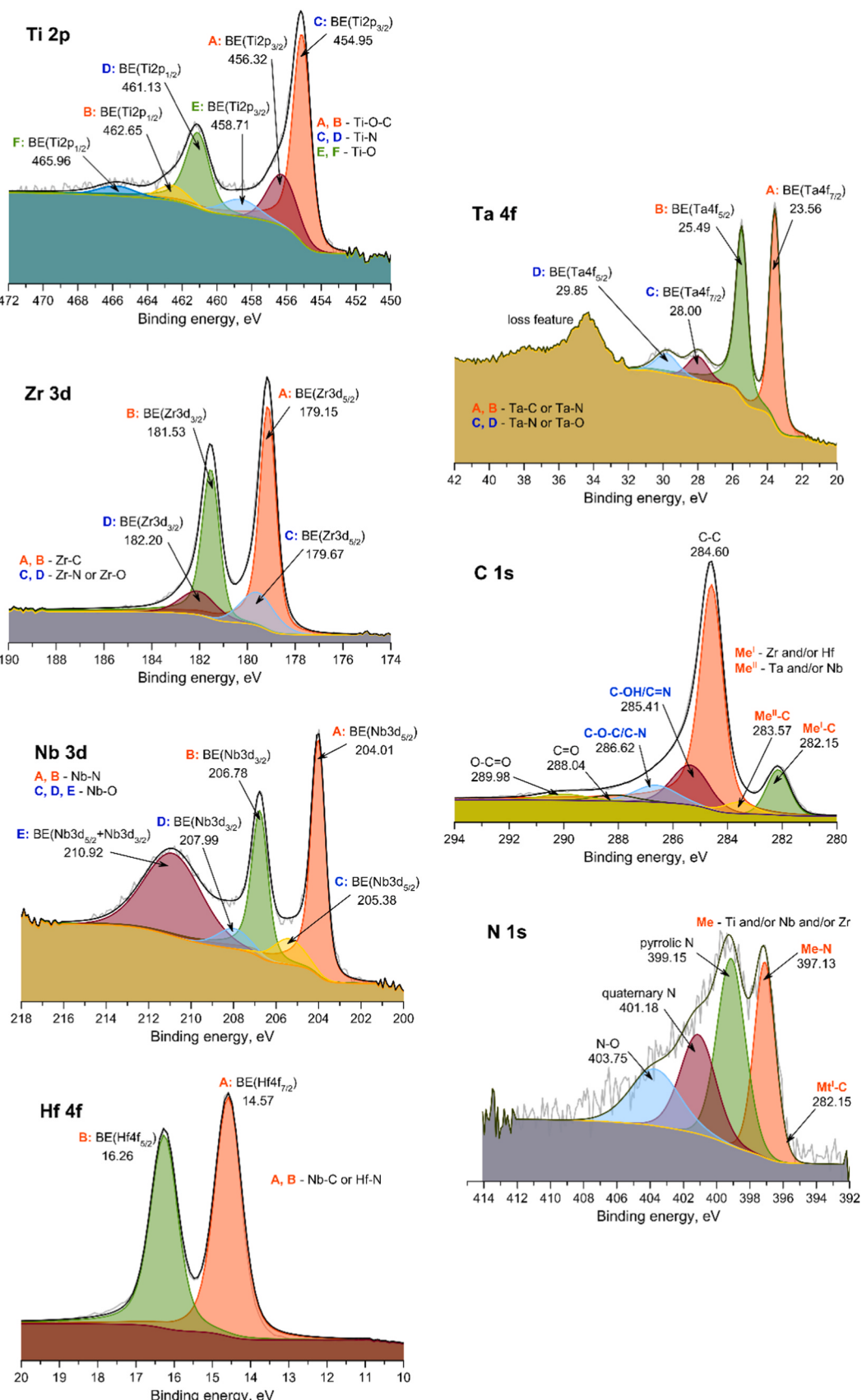


**Fig. 5.** XPS spectra of Ti2p, Zr3d, Nb3d, Hf4f, Ta4f, C1s, N1s for the product with the highest initial nitrogen content (presumably HEN). Background subtracted with Shirley function.

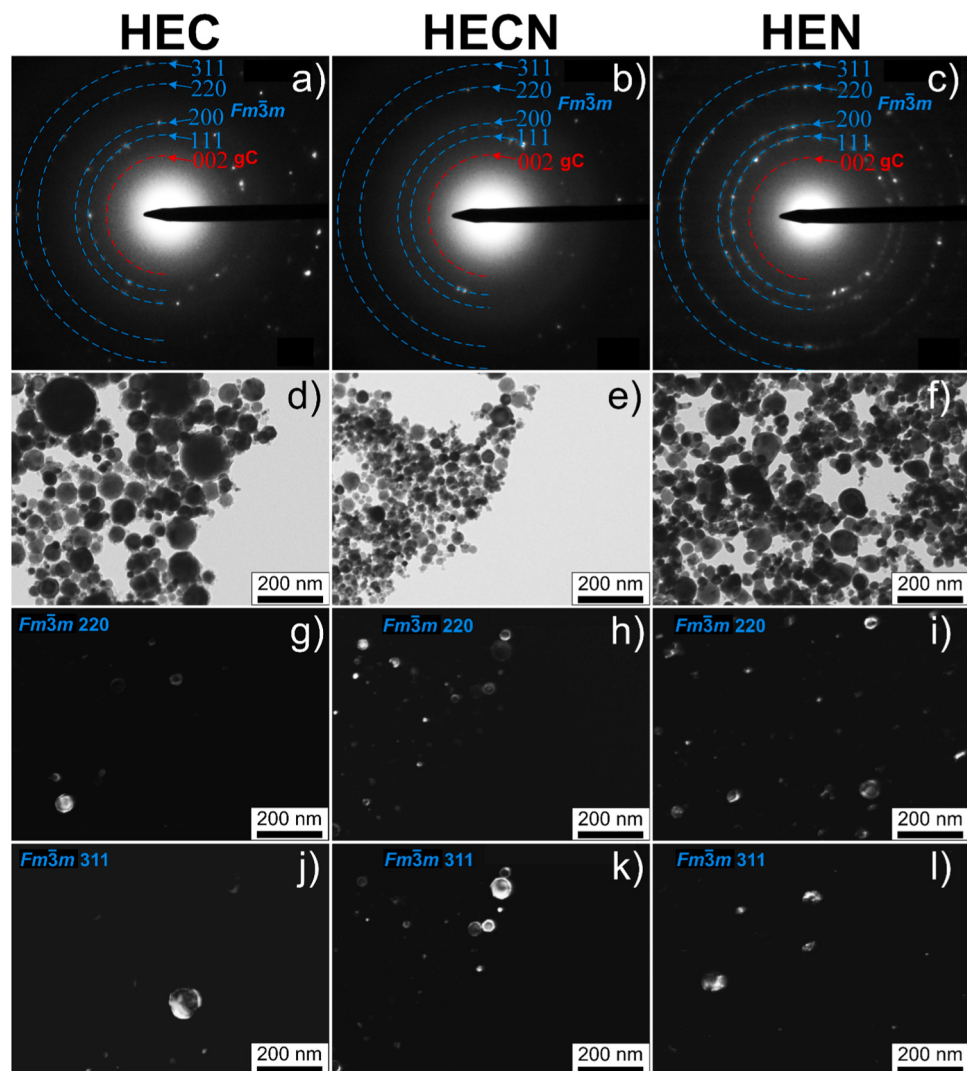


**Fig. 6.** Transmission electron microscopy analysis of the synthesized HEC, HECH, and HEN samples: (a–c) SAED, (d–f) bright-field TEM images. Dark-field TEM images with aperture shifted to the region of reflections corresponding to the (g–i) (220) and (j–l) (311) reflections of  $Fm\bar{3}m$  phases.

structures in free form is also confirmed by Raman and XPS analyses (Fig. 4 and Fig. 5). At the same time, there are no point reflections in the halo region indicating a complete representation of carbon in the form of graphite or graphene structures. Such structures are most likely present in the form of nanometer-thin films (well translucent electron beam objects) covering the surface of single crystal particles of the synthesized high-entropy cubic phase, which is particularly visible in TEM images (Fig. 1, Supporting information Y). Previously, the authors demonstrated the formation of similar halo structures when in the preparation of other carbides of refractory metals [70,101].

Carbon structures are most evident in the form of transparent shells during the synthesis of HEC in an argon atmosphere (Fig. 6d). Such shells are the main features of the synthesis of carbides using the electric discharges and plasma [102–104]. Such carbon structures are significantly reduced during synthesis in nitrogen atmosphere (Fig. 6e), especially without depositing additional carbon in the plasma structure formation channel (Fig. 6f). The smaller amount of excess carbon avoids the formation of pure carbides and allows the formation of nitrogen-containing structure.

#### 4. Conclusion

The application of the plasma dynamic technique to the synthesis of

high-entropy carbides and carbonitrides results in the formation of high-quality monophase powders. This method not only allows the efficient production of pure high-entropy carbide  $TiZrNbHfTaC_5$  in dispersed single crystal form, but also ensures the introduction of nitrogen into the crystal lattice, thereby synthesizing structures close to carbonitride. By using a carbon-free mixture of precursors in a nitrogen-containing gas atmosphere, it is possible to obtain materials containing up to 8 wt% nitrogen. The proposed mathematical model and the corresponding calculation provided a basis to explain the formation of high-entropy carbides and carbonitrides in the considered physical conditions. The implementation of a single-stage pulse (< 1 ms) thermal plasma process leads to the selective formation of nano-sized single-phase crystals of  $(TiZrNbHfTa)C_xN_y$  from different precursors, including pure metals and their oxides. The presented technique provides a simple and universal way to produce nanomaterials that can be used as constructive elements of oxygen-free UHTCs.

#### Author Contributions

A.G.K., A.Y.P. conceived this project. A.A.S. provided general idea of plasma dynamic method. I.I.S. performed a series of experiments on the synthesis of powders. D.S.N. performed experiments with microscopy analysis. A.Y.P. made X-ray diffraction analysis during whole study. A.N.

carried out thermal analysis of obtained powders. N.A.M., Y.A.K. performed theoretical calculations of Gibbs free energies, lattice constants, V.B.S. performed calculations with deep neural network potentials. A.G. K. prepared the analysis of results and wrote the manuscript. All the authors provided critical feedback and helped shape the research.

### CRediT authorship contribution statement

**Alexander A. Sivkov:** Resources, Formal analysis, Data curation. **Artur R. Nassyrbayev:** Methodology, Investigation, Formal analysis, Data curation. **Ivan I. Shannenkov:** Writing – review & editing, Writing – original draft, Visualization, Validation, Methodology, Investigation, Formal analysis. **Dmitry S. Nikitin:** Writing – review & editing, Writing – original draft, Validation, Resources, Methodology, Investigation. **Alexander G. Kvashnin:** Writing – review & editing, Writing – original draft, Supervision, Methodology, Investigation, Formal analysis, Conceptualization. **Alexander Ya. Pak:** Writing – review & editing, Writing – original draft, Supervision, Resources, Methodology, Investigation, Conceptualization. **Nikita A. Matsokin:** Writing – original draft, Methodology, Investigation, Formal analysis, Data curation. **Yulia A. Kvashnina:** Visualization, Software, Formal analysis, Data curation. **Viktor S. Baidyshev:** Writing – original draft, Visualization, Validation, Software, Methodology, Formal analysis, Data curation.

### Declaration of Competing Interest

The authors declare that they have no known competing financial interests or personal relationships that could have appeared to influence the work reported in this paper.

### Acknowledgements

Experimental studies on the plasma dynamic synthesis of single and high-entropy carbides in a dispersed form were supported by the Russian Science Foundation [grant number 23–73–01203, <https://rscf.ru/project/23-73-01203>]. Scanning and transmission electron microscopy was conducted with the application of equipment of the Tomsk Regional Core Shared Research Facilities Centre of National Research Tomsk State University. XPS measurements were carried out at the Central laboratories of Tomsk Polytechnic University (Analytical Center).

### Appendix A. Supporting information

Supplementary data associated with this article can be found in the online version at [doi:10.1016/j.jallcom.2024.177178](https://doi.org/10.1016/j.jallcom.2024.177178).

### Data Availability

Data will be made available on request.

### References

- [1] X. Jiao, Q. He, Q. Tan, X. Yin, Ablation behavior of mullite modified C/C-SiC-HfC composites under oxyacetylene torch for single and cyclic ablations with two heat fluxes, *J. Eur. Ceram. Soc.* 43 (2023) 5851–5862, <https://doi.org/10.1016/j.jeurceramsoc.2023.06.058>.
- [2] Q. Tan, X. Jiao, Q. He, Y. Wang, X. Yin, Effect of mullite content on microstructure and ablation behavior of mullite modified C/C-SiC-HfC composites, *Corros. Sci.* 222 (2023) 111405, <https://doi.org/10.1016/j.corsci.2023.111405>.
- [3] P. Sarker, T. Harrington, C. Toher, C. Oses, M. Samiee, J.-P. Maria, D.W. Brenner, K.S. Vecchio, S. Curtarolo, High-entropy high-hardness metal carbides discovered by entropy descriptors, *Nat. Commun.* 9 (2018) 4980, <https://doi.org/10.1038/s41467-018-07160-7>.
- [4] W. Zhang, D. Yan, W. Lu, Z. Li, Carbon and nitrogen co-doping enhances phase stability and mechanical properties of a metastable high-entropy alloy, *J. Alloy. Compd.* 831 (2020) 154799, <https://doi.org/10.1016/j.jallcom.2020.154799>.
- [5] P. Zhang, X. Liu, A. Cai, Q. Du, X. Yuan, H. Wang, Y. Wu, S. Jiang, Z. Lu, High-entropy carbide-nitrides with enhanced toughness and sinterability, *Sci. China Mater.* 64 (2021) 2037–2044, <https://doi.org/10.1007/s40843-020-1610-9>.
- [6] J.-W. Yeh, S.-K. Chen, S.-J. Lin, J.-Y. Gan, T.-S. Chin, T.-T. Shun, C.-H. Tsau, S.-Y. Chang, Nanostructured High-Entropy Alloys with Multiple Principal Elements: Novel Alloy Design Concepts and Outcomes, *Adv. Eng. Mater.* 6 (2004) 299–303, <https://doi.org/10.1002/adem.200300567>.
- [7] B. Cantor, I.T.H. Chang, P. Knight, A.J.B. Vincent, Microstructural development in equiatomic multicomponent alloys, *Mater. Sci. Eng.: A* 375–377 (2004) 213–218, <https://doi.org/10.1016/j.msea.2003.10.257>.
- [8] C. Toher, C. Oses, D. Hicks, S. Curtarolo, Unavoidable disorder and entropy in multi-component systems, *Npj Comput. Mater.* 5 (2019) 1–3, <https://doi.org/10.1038/s41524-019-0206-z>.
- [9] C.M. Rost, E. Sachet, T. Borman, A. Moballegh, E.C. Dickey, D. Hou, J.L. Jones, S. Curtarolo, J.-P. Maria, Entropy-stabilized oxides, *Nat. Commun.* 6 (2015) 8485, <https://doi.org/10.1038/ncomms9485>.
- [10] D.A. Vinnik, E.A. Trofimov, V.E. Zhivilin, O.V. Zaitseva, S.A. Gudkova, A. Yu Starikov, D.A. Zherebtsov, A.A. Kirsanova, M. Häßner, R. Niewa, High-entropy oxide phases with magnetoplumbite structure, *Ceram. Int.* 45 (2019) 12942–12948, <https://doi.org/10.1016/j.ceramint.2019.03.221>.
- [11] D. Wang, Z. Liu, S. Du, Y. Zhang, H. Li, Z. Xiao, W. Chen, R. Chen, Y. Wang, Y. Zou, S. Wang, Low-temperature synthesis of small-sized high-entropy oxides for water oxidation, *J. Mater. Chem. A* 7 (2019) 24211–24216, <https://doi.org/10.1039/C9TA08740K>.
- [12] A.H. Phakatkar, M.T. Saray, M.G. Rasul, L.V. Sorokina, T.G. Ritter, T. Shokuhfar, R. Shahbazian-Yassar, Ultrafast Synthesis of High Entropy Oxide Nanoparticles by Flame Spray Pyrolysis, *Langmuir* 37 (2021) 9059–9068, <https://doi.org/10.1021/acs.langmuir.1c01105>.
- [13] T.D. Desissa, M. Meja, D. Andoshe, F. Olu, F. Gochole, G. Bekele, O.A. Zelekew, T. Temesgen, B. Brehane, K.D. Kuffi, T. Hunde, Synthesis and characterizations of (Mg, Co, Ni, Cu, Zn)O high-entropy oxides, *SN Appl. Sci.* 3 (2021) 733, <https://doi.org/10.1007/s42452-021-04724-z>.
- [14] M. Anandkumar, E. Trofimov, Synthesis, Properties, and Applications of High-Entropy Oxide Ceramics: Current Progress and Future Perspectives, *J. Alloy. Compd.* (2023) 170690, <https://doi.org/10.1016/j.jallcom.2023.170690>.
- [15] D. Liu, T. Wen, B. Ye, Y. Chu, Synthesis of superfine high-entropy metal diboride powders, *Scr. Mater.* 167 (2019) 110–114, <https://doi.org/10.1016/j.scriptamat.2019.03.038>.
- [16] Y. Zhang, S.-K. Sun, W.-M. Guo, W. Zhang, L. Xu, J.-H. Yuan, D.-K. Guan, D.-W. Wang, Y. You, H.-T. Lin, Fabrication of textured (Hf0.2Zr0.2Ta0.2Cr0.2Ti0.2)B2 high-entropy ceramics, *J. Eur. Ceram. Soc.* 41 (2021) 1015–1019, <https://doi.org/10.1016/j.jeurceramsoc.2020.08.071>.
- [17] B. Storr, D. Kodali, K. Chakrabarty, P.A. Baker, V. Rangari, S.A. Catledge, Single-Step Synthesis Process for High-Entropy Transition Metal Boride Powders Using Microwave Plasma, *Ceramics* 4 (2021) 257–264, <https://doi.org/10.3390/ceramics4020020>.
- [18] X. Zhang, W. Li, H. Tian, J. Liu, C. Li, H. Dong, J. Chen, M. Song, B. Chen, H. Sheng, S. Wang, D. Zhang, H. Zhang, Ultra-incompressible High-Entropy Diborides, *J. Phys. Chem. Lett.* 12 (2021) 3106–3113, <https://doi.org/10.1021/acs.jpclett.1c03399>.
- [19] B. Storr, L. Moore, K. Chakrabarty, Z. Mohammed, V. Rangari, C.-C. Chen, S. A. Catledge, Properties of high entropy borides synthesized via microwave-induced plasma, *APL Mater.* 10 (2022) 061109, <https://doi.org/10.1063/5.0098276>.
- [20] S. Iwan, C. Perreault, Y.K. Vohra, Synthesis and Ultrahigh Pressure Compression of High-Entropy Boride (Hf0.2Mo0.2Nb0.2Ta0.2Zr0.2)B2 to 220 GPa, *Materials* 16 (2023) 158, <https://doi.org/10.3390/ma16010158>.
- [21] T.J. Harrington, J. Gild, P. Sarker, C. Toher, C.M. Rost, O.F. Dippo, C. McElfresh, K. Kaufmann, E. Marin, L. Borowski, P.E. Hopkins, J. Luo, S. Curtarolo, D. W. Brenner, K.S. Vecchio, Phase stability and mechanical properties of novel high entropy transition metal carbides, *Acta Mater.* 166 (2019) 271–280, <https://doi.org/10.1016/j.actamat.2018.12.054>.
- [22] S. Guan, H. Liang, Q. Wang, L. Tan, F. Peng, Synthesis and Phase Stability of the High-Entropy Carbide (Ti0.2Zr0.2Nb0.2Ta0.2Mo0.2)C under Extreme Conditions, *Inorg. Chem.* 60 (2021) 3807–3813, <https://doi.org/10.1021/acs.inorgchem.0c03319>.
- [23] S. Kaval, K.G. Bayrak, M. Bellek, S. Mertdinç, F. Muhaffel, H. Gökc, E. Ayas, B. Derin, M.L. Öveçoğlu, D. Ağaoğulları, Synthesis and characterization of (HfMoTiWZr)C high entropy carbide ceramics, *Ceram. Int.* 48 (2022) 7695–7705, <https://doi.org/10.1016/j.ceramint.2021.11.317>.
- [24] A.Y. Pak, V. Sotskov, A.A. Gumovskaya, Y.Z. Vassilyeva, Z.S. Bolatova, Y. A. Kvashnina, G.Y. Mamontov, A.V. Shapeev, A.G. Kvashnina, Machine learning-driven synthesis of TiZrNbHfTaC5 high-entropy carbide, *Npj Comput. Mater.* 9 (2023) 1–11, <https://doi.org/10.1038/s41524-022-00955-9>.
- [25] A. Bao, J. Wu, Y. Zhang, X. Wang, X. Zhang, Y. Gu, X. Qi, Facile synthesis of metal carbides with high-entropy strategy for engineering electrical properties, *J. Mater. Res. Technol.* 23 (2023) 1312–1320, <https://doi.org/10.1016/j.jmrt.2023.01.053>.
- [26] J. Gild, J. Braun, K. Kaufmann, E. Marin, T. Harrington, P. Hopkins, K. Vecchio, J. Luo, A high-entropy silicide: (Mo0.2Nb0.2Ta0.2Ti0.2W0.2Si2, *J. Mater.* 5 (2019) 337–343, <https://doi.org/10.1016/j.jmat.2019.03.002>.
- [27] Y. Qin, J.-X. Liu, F. Li, X. Wei, H. Wu, G.-J. Zhang, A high entropy silicide by reactive spark plasma sintering, *J. Adv. Ceram.* 8 (2019) 148–152, <https://doi.org/10.1007/s40145-019-0319-3>.

- [28] L. Liu, L. Zhang, D. Liu, Complete elimination of pest oxidation by high entropy refractory metallic silicide ( $\text{Mo}_{0.2}\text{W}_{0.2}\text{Cr}_{0.2}\text{Ta}_{0.2}\text{Nb}_{0.2}\text{Si}_2$ ), *Scr. Mater.* 189 (2020) 25–29, <https://doi.org/10.1016/j.scriptamat.2020.07.059>.
- [29] J. Kuang, P. Zhang, Q. Wang, Z. Hu, X. Liang, B. Shen, Formation and oxidation behavior of refractory high-entropy silicide ( $\text{NbMoTaW}\text{Si}_2$ ) coating, *Corros. Sci.* 198 (2022) 110134, <https://doi.org/10.1016/j.corsci.2022.110134>.
- [30] R.-Z. Zhang, F. Gucci, H. Zhu, K. Chen, M.J. Reece, Data-Driven Design of Ecofriendly Thermoelectric High-Entropy Sulfides, *Inorg. Chem.* 57 (2018) 13027–13033, <https://doi.org/10.1021/acs.inorgchem.8b02379>.
- [31] L. Lin, K. Wang, A. Sarkar, C. Njel, G. Karkera, Q. Wang, R. Azmi, M. Fichtner, H. Hahn, S. Schweidler, B. Breitung, High-Entropy Sulfides as Electrode Materials for Li-Ion Batteries, *Adv. Energy Mater.* 12 (2022) 2103090, <https://doi.org/10.1002/aenm.202103090>.
- [32] M. Moradi, F. Hasanzadian, A. Bahadoran, A. Shokri, S. Zerangnasrabad, B. Kakavandi, New high-entropy transition-metal sulfide nanoparticles for electrochemical oxygen evolution reaction, *Electrochim. Acta* 436 (2022) 141444, <https://doi.org/10.1016/j.electacta.2022.141444>.
- [33] T. Jin, X. Sang, R.R. Unocic, R.T. Kinch, X. Liu, J. Hu, H. Liu, S. Dai, Mechanoochemical-Assisted Synthesis of High-Entropy Metal Nitride via a Soft Urea Strategy, *Adv. Mater.* 30 (2018) 1707512, <https://doi.org/10.1002/adma.201707512>.
- [34] O.F. Dippo, N. Mesgarzadeh, T.J. Harrington, G.D. Schrader, K.S. Vecchio, Bulk high-entropy nitrides and carbonitrides, *Sci. Rep.* 10 (2020) 21288, <https://doi.org/10.1038/s41598-020-78175-8>.
- [35] D. Moskovskikh, S. Vorotilo, V. Buinevich, A. Sedegov, K. Kuskov, A. Khort, C. Shuck, M. Zhukovsky, A. Mukasyan, Extremely hard and tough high entropy nitride ceramics, *Sci. Rep.* 10 (2020) 19874, <https://doi.org/10.1038/s41598-020-76945-y>.
- [36] V. Novikov, N. Stepanov, S. Zherebtsov, G. Salishchev, Structure and Properties of High-Entropy Nitride Coatings, *Metals* 12 (2022) 847, <https://doi.org/10.3390/met12050847>.
- [37] D. Ni, Y. Cheng, J. Zhang, J.-X. Liu, J. Zou, B. Chen, H. Wu, H. Li, S. Dong, J. Han, X. Zhang, Q. Fu, G.-J. Zhang, Advances in ultra-high temperature ceramics, composites, and coatings, *J. Adv. Ceram.* 11 (2022) 1–56, <https://doi.org/10.1007/s40145-021-0550-6>.
- [38] A. Lynch, A.R. Romero, F. Xu, R.W. Wellman, T. Hussain, Thermal Spraying of Ultra-High Temperature Ceramics: A Review on Processing Routes and Performance, *J. Therm. Spray. Tech.* 31 (2022) 745–779, <https://doi.org/10.1007/s11666-022-01381-5>.
- [39] K. Xiong, L. Yang, F. Wang, S. Zhang, L. You, H. Wu, Y. Mao, A first-principles study the effects of nitrogen on the lattice distortion, mechanical, and electronic properties of ( $\text{ZrHfNbTa}$ ) $\text{Cl}_{1-x}\text{N}$  high entropy carbonitrides, *J. Alloy. Compd.* 930 (2023) 167378, <https://doi.org/10.1016/j.jallcom.2022.167378>.
- [40] Z. Wang, Z.-T. Li, S.-J. Zhao, Z.-G. Wu, High-entropy carbide ceramics: a perspective review, *Tungsten* 3 (2021) 131–142, <https://doi.org/10.1007/s42864-021-00085-7>.
- [41] Z. Cao, J. Sun, L. Meng, K. Zhang, J. Zhao, Z. Huang, X. Yun, Progress in densification and toughening of high entropy carbide ceramics, *J. Mater. Sci. Technol.* 161 (2023) 10–43, <https://doi.org/10.1016/j.jmst.2023.03.034>.
- [42] S. Yudin, S. Volodko, D. Moskovskikh, I. Alimov, A. Guryanov, S. Zhevnenko, H. Guo, A. Korotitsky, K. Sidnov, S. Roslyakov, C. Zhang, Fabrication of high-entropy carbide ceramics ( $\text{Ti},\text{Zr},\text{Hf},\text{Nb},\text{Ta}$ ) $\text{C}$  through low-temperature calcium-hydride reduction of oxides, *J. Eur. Ceram. Soc.* 43 (2023) 5108–5116, <https://doi.org/10.1016/j.jeurceramsoc.2023.04.056>.
- [43] K. Lu, J.-X. Liu, X.-F. Wei, W. Bao, Y. Wu, F. Li, F. Xu, G.-J. Zhang, Microstructures and mechanical properties of high-entropy ( $\text{Ti}_{0.2}\text{Zr}_{0.2}\text{Hf}_{0.2}\text{Nb}_{0.2}\text{Ta}_{0.2}\text{C}$ ) $\text{C}$  ceramics with the addition of SiC secondary phase, *J. Eur. Ceram. Soc.* 40 (2020) 1839–1847, <https://doi.org/10.1016/j.jeurceramsoc.2019.12.056>.
- [44] X. Han, V. Girman, R. Sedlak, J. Dusza, E.G. Castle, Yichen Wang, M. Reece, C. Zhang, Improved creep resistance of high entropy transition metal carbides, *J. Eur. Ceram. Soc.* 40 (2020) 2709–2715, <https://doi.org/10.1016/j.jeurceramsoc.2019.12.036>.
- [45] X.Q. Han, N. Lin, A.Q. Li, J.Q. Li, Z.G. Wu, Z.Y. Wang, Y.H. He, X.Y. Kang, C. Ma, Microstructure and characterization of ( $\text{Ti},\text{V},\text{Nb},\text{Ta},\text{C}$ ) $\text{N}$  high-entropy ceramic, *Ceram. Int.* 47 (2021) 35105–35110, <https://doi.org/10.1016/j.ceramint.2021.09.053>.
- [46] C. Jing, S.-J. Zhou, W. Zhang, Z.-Y. Ding, Z.-G. Liu, Y.-J. Wang, J.-H. Ouyang, Low temperature synthesis and densification of ( $\text{Ti},\text{V},\text{Nb},\text{Ta},\text{Mo}$ ) $\text{C}$  $\text{N}$  high-entropy carbonitride ceramics, *J. Alloy. Compd.* 927 (2022) 167095, <https://doi.org/10.1016/j.jallcom.2022.167095>.
- [47] S. Ma, J. Ma, Z. Yang, Y. Gong, K. Li, G. Yu, Z. Xue, Synthesis of novel single-phase high-entropy metal carbonitride ceramic powders, *Int. J. Refract. Met. Hard Mater.* 94 (2021) 105390, <https://doi.org/10.1016/j.ijrmhm.2020.105390>.
- [48] T. Wen, B. Ye, M.C. Nguyen, M. Ma, Y. Chu, Thermophysical and mechanical properties of novel high-entropy metal nitride-carbides, *J. Am. Ceram. Soc.* 103 (2020) 6475–6489, <https://doi.org/10.1111/jace.17333>.
- [49] A.Ya Pak, V.V. Uglow, V.A. Skuratov, A.A. Svinikhova, P.V. Povalyaev, A. P. Korchagina, Synthesis of  $\text{TiZrNbHfTaC}_5$  High-Entropy Carbide Powder: Sintering and Radiation Resistance Research, *Russ. Phys. J.* 67 (2024) 489–495, <https://doi.org/10.1007/s11182-024-03148-7>.
- [50] S.-Y. Liu, S. Zhang, S. Liu, D.-J. Li, Y. Li, S. Wang, Phase stability, mechanical properties and melting points of high-entropy quaternary metal carbides from first-principles, *J. Eur. Ceram. Soc.* 41 (2021) 6267–6274, <https://doi.org/10.1016/j.jeurceramsoc.2021.05.022>.
- [51] S.-Y. Liu, C. Liu, S. Zhang, S. Liu, D.-J. Li, Y. Li, S. Wang, Phase diagram and mechanical properties of fifteen quaternary high-entropy metal diborides: First-principles calculations and thermodynamics, *J. Appl. Phys.* 131 (2022) 075105, <https://doi.org/10.1063/5.0079808>.
- [52] P. Hohenberg, W. Kohn, Inhomogeneous electron gas, *Phys. Rev.* 136 (1964) B864–B871.
- [53] W. Kohn, L.J. Sham, Self-consistent equations including exchange and correlation effects, *Phys. Rev.* 140 (1965) A1133–A1138.
- [54] J.P. Perdew, K. Burke, M. Ernzerhof, Generalized gradient approximation made simple, *Phys. Rev. Lett.* 77 (1996) 3865–3868.
- [55] P.E. Blöchl, Projector augmented-wave method, *Phys. Rev. B* 50 (1994) 17953–17979, <https://doi.org/10.1103/PhysRevB.50.17953>.
- [56] G. Kresse, D. Joubert, From ultrasoft pseudopotentials to the projector augmented-wave method, *Phys. Rev. B* 59 (1999) 1758–1775, <https://doi.org/10.1103/PhysRevB.59.1758>.
- [57] G. Kresse, J. Hafner, Ab initio molecular dynamics for liquid metals, *Phys. Rev. B* 47 (1993) 558–561.
- [58] G. Kresse, J. Hafner, Ab initio molecular-dynamics simulation of the liquid-metal-amorphous-semiconductor transition in germanium, *Phys. Rev. B* 49 (1994) 14251–14269.
- [59] G. Kresse, J. Furthmüller, Efficient iterative schemes for ab initio total-energy calculations using a plane-wave basis set, *Phys. Rev. B* 54 (1996) 11169–11186.
- [60] M. Methfessel, A.T. Paxton, High-precision sampling for Brillouin-zone integration in metals, *Phys. Rev. B* 40 (1989) 3616–3621, <https://doi.org/10.1103/PhysRevB.40.3616>.
- [61] G. Kern, G. Kresse, J. Hafner, Ab Initio Calculation of the Lattice Dynamics and Phase Diagram of Boron Nitride, *Phys. Rev. B* 59 (1999) 8551–8559, <https://doi.org/10.1103/PhysRevB.59.8551>.
- [62] A. Togo, I. Tanaka, First principles phonon calculations in materials science, *Scr. Mater.* 108 (2015) 1–5, <https://doi.org/10.1016/j.scriptamat.2015.07.021>.
- [63] A. Togo, F. Oba, I. Tanaka, First-principles calculations of the ferroelastic transition between rutile-type and  $\text{CaCl}_2$ -type  $\text{SiO}_2$  at high pressures, *Phys. Rev. B* 78 (2008) 134106, <https://doi.org/10.1103/PhysRevB.78.134106>.
- [64] V. Wang, N. Xu, J.-C. Liu, G. Tang, W.-T. Geng, VASPKIT: A user-friendly interface facilitating high-throughput computing and analysis using VASP code, *Comput. Phys. Commun.* 267 (2021) 108033, <https://doi.org/10.1016/j.cpc.2021.108033>.
- [65] S. Plimpton, Fast Parallel Algorithms for Short-Range Molecular Dynamics, *J. Comp. Phys.* 117 (1995) 1–19.
- [66] H. Wang, L. Zhang, J. Han, W. E, DeePMD-kit: A deep learning package for many-body potential energy representation and molecular dynamics, *Comput. Phys. Commun.* 228 (2018) 178–184, <https://doi.org/10.1016/j.cpc.2018.03.016>.
- [67] S. Nosé, A unified formulation of the constant temperature molecular dynamics methods, *J. Chem. Phys.* 81 (1984) 511–519, <https://doi.org/10.1063/1.447334>.
- [68] W.G. Hoover, Canonical dynamics: Equilibrium phase-space distributions, *Phys. Rev. A* 31 (1985) 1695–1697, <https://doi.org/10.1103/PhysRevA.31.1695>.
- [69] A. Sivkov, Y. Vympina, A. Ivashutenko, I. Rahmatullin, Y. Shanenkova, D. Nikitin, I. Shanenkova, Plasma dynamic synthesis of highly defective fine titanium dioxide with tunable phase composition, *Ceram. Int.* 48 (2022) 10862–10873, <https://doi.org/10.1016/j.ceramint.2021.12.303>.
- [70] A.G. Kvashnin, D.S. Nikitin, I.I. Shanenkova, I.V. Chepkasov, Y.A. Kvashnina, A. Nassyrbayev, A.A. Sivkov, Z. Bolatova, A.Ya Pak, Large-Scale Synthesis and Applications of Hafnium-Tantalum Carbides, *Adv. Funct. Mater.* 32 (2022) 2206289, <https://doi.org/10.1002/adfm.202206289>.
- [71] A.A. Sivkov, D.Yu Gerasimov, D.S. Nikitin, Synthesis of Nanocrystalline Titanium Diboride in a Hypervelocity Plasma Jet, *Tech. Phys. Lett.* 44 (2018) 301–304, <https://doi.org/10.1134/S1063785018040090>.
- [72] S.V. Bobashev, B.G. Zhukov, R.A. Kurakin, S.A. Ponyaev, B.I. Reznikov, S. I. Rozov, Parameters of an erosion carbon plasma in the channel of a railgun, *Tech. Phys.* 55 (2010) 1754–1759, <https://doi.org/10.1134/S1063784210200788>.
- [73] I. Shanenkova, D. Nikitin, A. Ivashutenko, I. Rahmatullin, Y. Shanenkova, A. Nassyrbayev, W. Han, A. Sivkov, Hardening the surface of metals with  $\text{WC}_{1-x}$  coatings deposited by high-speed plasma spraying, *Surf. Coat. Technol.* 389 (2020) 125639, <https://doi.org/10.1016/j.surfcoat.2020.125639>.
- [74] A.A. Sivkov, D.S. Nikitin, A.Ya Pak, I.A. Rahmatullin, Influence of plasmodynamic synthesis energy in Si-C system on the product phase composition and dispersion, *Nanotechnol. Russ.* 10 (2015) 34–41, <https://doi.org/10.1134/S1995078015010188>.
- [75] A. Pak, A. Sivkov, I. Shanenkova, I. Rahmatullin, K. Shatrova, Synthesis of ultrafine cubic tungsten carbide in a discharge plasma jet, *Int. J. Refract. Met. Hard Mater.* 48 (2015) 51–55, <https://doi.org/10.1016/j.ijrmhm.2014.07.025>.
- [76] B. Hafner, Scanning electron microscopy primer, Characterization Facility, University of Minnesota-Twin Cities (2007) 1–29.
- [77] X. Yang, Y. Zhang, Prediction of high-entropy stabilized solid-solution in multi-component alloys, *Mater. Chem. Phys.* 132 (2012) 233–238, <https://doi.org/10.1016/j.matchemphys.2011.11.021>.
- [78] J. Zhang, A.R. Ogano, X. Li, H. Niu, Pressure-stabilized hafnium nitrides and their properties, *Phys. Rev. B* 95 (2017) 020103, <https://doi.org/10.1103/PhysRevB.95.020103>.
- [79] S.H. Elder, F.J. DiSalvo, L. Topor, A. Navrotsky, Thermodynamics of ternary nitride formation by ammonolysis: application to lithium molybdenum nitride ( $\text{LiMoN}_2$ ), sodium tungsten nitride ( $\text{Na}_3\text{WN}_3$ ), and sodium tungsten oxide nitride ( $\text{Na}_3\text{WO}_3\text{N}$ ), *Chem. Mater.* 5 (1993) 1545–1553, <https://doi.org/10.1021/cm00034a027>.

- [80] A.N. Kornilov, N.V. Chelovskaya, V.I. Zhelankin, G.P. Shveikin, Enthalpies of formation of hafnium carbides, *J. Chem. Thermodyn.* 9 (1977) 629–642, [https://doi.org/10.1016/0021-9614\(77\)90088-X](https://doi.org/10.1016/0021-9614(77)90088-X).
- [81] H. Okamoto, The Hf-N (Hafnium-Nitrogen) system, *Bull. Alloy Phase Diagr.* 11 (1990) 146–149, <https://doi.org/10.1007/BF02841699>.
- [82] A.V. Pshyk, A. Vasylenko, B. Bakhit, L. Hultman, P. Schweizer, T.E.J. Edwards, J. Michler, G. Greczynski, High-entropy transition metal nitride thin films alloyed with Al: Microstructure, phase composition and mechanical properties, *Mater. Des.* 219 (2022) 110798, <https://doi.org/10.1016/j.matdes.2022.110798>.
- [83] A.D. Pogrebnyak, A.A. Bagdasaryan, I.V. Yakushchenko, V.M. Beresnev, The structure and properties of high-entropy alloys and nitride coatings based on them, *Russ. Chem. Rev.* 83 (2014) 1027, <https://doi.org/10.1070/RCR4407>.
- [84] J.A. Dean, *Lange's handbook of chemistry*, McGraw-Hill, New York, N.Y., 1999.
- [85] G. Gassner, P.H. Mayrhofer, C. Mitterer, J. Kiefer, Structure–property relations in Cr–C/a-C:H coatings deposited by reactive magnetron sputtering, *Surf. Coat. Technol.* 200 (2005) 1147–1150, <https://doi.org/10.1016/j.surfcoat.2005.02.186>.
- [86] J. Li, Q. Zhang, S. Chen, H. Fan, J. Song, Y. Su, L. Hu, Y. Zhou, Y. Zhang, Carbon-deficient high-entropy (Zr0.17Nb0.2Ta0.2Mo0.2W0.2)C0.89: A potential high temperature and vacuum wear-resistant material, *Mater. Des.* 226 (2023) 111680, <https://doi.org/10.1016/j.matdes.2023.111680>.
- [87] P.M. Brune, G.E. Hilmas, W.G. Fahrenholz, J.L. Watts, C.J. Ryan, C.M. DeSalle, D.E. Wolfe, S. Curtarolo, Hardness of single phase high entropy carbide ceramics with different compositions, *J. Appl. Phys.* 135 (2024) 165106, <https://doi.org/10.1063/5.0198141>.
- [88] M.D. Hossain, T. Borman, A. Kumar, X. Chen, A. Khosrovani, S.R. Kalidindi, E. A. Paisley, M. Esters, C. Oses, C. Toher, S. Curtarolo, J.M. LeBeau, D. Brenner, J.-P. Maria, Carbon stoichiometry and mechanical properties of high entropy carbides, *Acta Mater.* 215 (2021) 117051, <https://doi.org/10.1016/j.actamat.2021.117051>.
- [89] V. Braic, M. Balaceanu, M. Braic, A. Vladescu, S. Panseri, A. Russo, Characterization of multi-principal-element (Ti<sub>x</sub>ZrNbHfTa)N and (Ti<sub>x</sub>ZrNbHfTa)C coatings for biomedical applications, *J. Mech. Behav. Biomed. Mater.* 10 (2012) 197–205, <https://doi.org/10.1016/j.jmbbm.2012.02.020>.
- [90] I. Carvalho, M. Henriques, J.C. Oliveira, C.F. Almeida Alves, A.P. Piedade, S. Carvalho, Influence of surface features on the adhesion of *Staphylococcus epidermidis* to Ag-TiCN thin films, *Sci. Technol. Adv. Mater.* 14 (2013) 035009, <https://doi.org/10.1088/1468-6996/14/3/035009>.
- [91] C. Oliveira, R.E. Galindo, C. Palacio, L. Vázquez, A. Espinosa, B.G. Almeida, M. Henriques, S.C. V, S. Carvalho, Influence of the surface morphology and microstructure on the biological properties of Ti–Si–C–N–O coatings, *Thin Solid Films* 518 (2010) 5694–5699, <https://doi.org/10.1016/j.tsfn.2010.05.050>.
- [92] I. Dreiling, A. Haug, H. Holzschuh, T. Chassé, Raman spectroscopy as a tool to study cubic Ti–C–N CVD coatings, *Surf. Coat. Technol.* 204 (2009) 1008–1012, <https://doi.org/10.1016/j.surfcoat.2009.05.029>.
- [93] N.K. Manninen, R.E. Galindo, N. Benito, N.M. Figueiredo, A. Cavaleiro, C. Palacio, S. Carvalho, Ag–Ti(C, N)-based coatings for biomedical applications: influence of silver content on the structural properties, *J. Phys. D: Appl. Phys.* 44 (2011) 375501, <https://doi.org/10.1088/0022-3727/44/37/375501>.
- [94] A.C. Ferrari, S.E. Rodil, J. Robertson, Resonant Raman spectra of amorphous carbon nitrides: the G peak dispersion, *Diam. Relat. Mater.* 12 (2003) 905–910, [https://doi.org/10.1016/S0925-9635\(02\)00370-9](https://doi.org/10.1016/S0925-9635(02)00370-9).
- [95] B.X. Huang, K. Wang, J.S. Church, Y.-S. Li, Characterization of oxides on niobium by raman and infrared spectroscopy, *Electrochim. Acta* 44 (1999) 2571–2577, [https://doi.org/10.1016/S0013-4686\(98\)00385-5](https://doi.org/10.1016/S0013-4686(98)00385-5).
- [96] J. Yuan, X. Zhou, S. Dong, J. Jiang, L. Deng, W. Song, D.B. Dingwell, X. Cao, Tailoring the initial characterization of fully stabilized HfO<sub>2</sub> with Y2O<sub>3</sub>/Ta<sub>2</sub>O<sub>5</sub>, *J. Alloy. Compd.* 867 (2021) 159113, <https://doi.org/10.1016/j.jallcom.2021.159113>.
- [97] A. Naumenko, Iu Gnatiuk, N. Smirnova, A. Eremenko, Characterization of sol-gel derived TiO<sub>2</sub>/ZrO<sub>2</sub> films and powders by Raman spectroscopy, *Thin Solid Films* 520 (2012) 4541–4546, <https://doi.org/10.1016/j.tsf.2011.10.189>.
- [98] B.V. Crist, *Handbook of Monochromatic XPS Spectra: The Elements of Native Oxides*, Wiley, 2000. (<https://www.wiley.com/en-us/Handbook+of+Monochromatic+XPS+Spectra%3A+The+Elements+of+Native+Oxides-p-9780471492658>) (accessed January 15, 2024).
- [99] bvcrist, The International XPS Database of XPS Reference Spectra, The International XPS Database 1 (n.d.). <https://xpsdatabase.com/> (accessed January 15, 2024).
- [100] J.-D. Gu, P.-L. Chen, Investigation of the corrosion resistance of ZrCN hard coatings fabricated by advanced controlled arc plasma deposition, *Surf. Coat. Technol.* 200 (2006) 3341–3346, <https://doi.org/10.1016/j.surfcoat.2005.07.049>.
- [101] I. Shanenkov, D. Nikitin, A. Ivashutenko, Y. Shanenkova, Y. Vympina, D. Butenko, W. Han, A. Sivkov, Studies on the thermal stability of nanosized powder of WC<sub>1-x</sub>-based product prepared by plasma dynamic method, compaction feasibility of the powder and preparation of composite with aluminium, *Ceram. Int.* 47 (2021) 6884–6895, <https://doi.org/10.1016/j.ceramint.2020.11.035>.
- [102] M.-H. Lin, Synthesis of nanophasse tungsten carbide by electrical discharge machining, *Ceram. Int.* 31 (2005) 1109–1115, <https://doi.org/10.1016/j.ceramint.2004.12.004>.
- [103] Z. Abdullaeva, E. Omurzak, C. Iwamoto, H. Okudera, M. Koinuma, S. Takebe, S. Sulaimankulova, T. Mashimo, High temperature stable WC<sub>1-x</sub>@C and TiC@C core–shell nanoparticles by pulsed plasma in liquid, *RSC Adv.* 3 (2012) 513–519, <https://doi.org/10.1039/C2RA22028H>.
- [104] P. Livan, T. Öztürk, Carbon encapsulation of elemental nanoparticles by spark discharge, *J. Mater. Sci.* 53 (2018) 14350–14360, <https://doi.org/10.1007/s10853-018-2647-z>.